Aleksandr Shkoruta[1]
Department of Mechanical, Aerospace, and Nuclear Engineering,
Rensselaer Polytechnic Institute,
Troy, NY 12180
e-mail: shkora@rpi.edu

Sandipan Mishra
Department of Mechanical, Aerospace, and Nuclear Engineering,
Rensselaer Polytechnic Institute,
Troy, NY 12180
e-mail: mishrs2@rpi.edu

Stephen J. Rock
Manufacturing Innovation Center,
Rensselaer Polytechnic Institute,
Troy, NY 12180
e-mail: rocks@rpi.edu

Real-Time Image-Based Feedback Control of Laser Powder Bed Fusion

This letter presents the design and experimental validation of a real-time image-based feedback control system for metal laser powder bed fusion (LPBF). A coaxial melt pool video stream is used to control laser power in real-time at 2 kHz. Modeling of the melt pool image response to changes in the input laser power is presented. Based on this identified model, a real-time feedback controller is implemented experimentally on a single track and part scales. On a single-track scale, the controller successfully tracks a time-varying melt pool reference. On a part-level scale, the controller successfully regulates the melt pool image signature to the desired reference value, reducing layer-to-layer signal variation and eliminating within-layer signal drift. [DOI: 10.1115/1.4051588]

Keywords: control applications, dynamics and control, identification, mechatronics, modeling, additive manufacturing, feedback, process control

1 Introduction

Laser powder bed fusion (LPBF)[2] is a metal additive manufacturing process. The typical LPBF system is shown in Fig. 1: a high-power laser scans the surface of the metal powder and selectively melts it in a layer-by-layer fashion. LPBF can produce fully functional metal parts of complex geometry, such as organic shapes or lattice structures. However, LPBF-produced parts are prone to defects, such as porosity or distortion. As a result, significant manual effort is required to dial in process parameters for a particular part [1].

The consensus in the existing literature is that LPBF can benefit from process monitoring and control [2]. LPBF monitoring has seen significant progress recently [3]. Particular attention has been devoted to the high-speed observation of the melt pool, as the melt pool is of prime importance for process quality outcomes [1]. In contrast, only a handful of controllers for LPBF have been experimentally demonstrated [2], major reasons being (1) the closed architecture of the commercial LPBF machines and (2) the stringent requirements on sensor resolution and system bandwidth [4]. The majority of published studies employ *feedforward* schemes, such as control of laser power based on local geometry [5], control of laser power based on a data-driven predictive model [6], control of a cross-sectional area of a bead on a plate [7], layer-to-layer control on a line-by-line basis [8], and layer-to-layer iterative learning control [9].

For *feedback* control of LPBF, the seminal work of Kruth et al. [10] hinted at the use of a camera in the feedback loop but did not provide details on the closed-loop control design. The subsequent work by Craeghs et al. [11] used only a photodiode signal to control the laser power. Another photodiode-based controller was recently reported by a different group of authors [12].

To the authors' best knowledge, substantial work on image-based melt pool monitoring has been reported in the literature, but a systematic study of real-time image-based feedback control of the LPBF process has not been reported. Thus, the key contributions of this work are as follows:

(1) design and implementation of a real-time control system integrating the melt pool imaging with real-time in-line laser power control on a custom LPBF testbed;
(2) experimental modeling of the melt pool image response to changes in the input laser power under a variety of conditions; and
(3) experimental validation of the melt pool reference tracking with a real-time feedback controller, on a single-track and multi-layer part-scale.

2 Experimental Setup

The results presented in this letter are based on the open-architecture LPBF testbed, described in Ref. [9]. The testbed follows the typical hardware architecture of the industrial LPBF machines (as in Fig. 1) and is capable of producing full-scale metal parts as large as $50 \times 50 \times 100$ mm. The testbed is instrumented with a near-infrared (NIR) camera that observes the melt pool through laser focusing optics. The setup is described in detail in Ref. [13] and is similar to Refs. [6,8,11,14]. In such a "coaxial" setup, the camera's field of view is always centered on the melt pool, which allows for a high spatio-temporal resolution. The camera's integration time is 400 μs, the sampling rate is 2 kHz, and the instantaneous field of view is 22 μm per pixel. A typical melt pool image is shown in Fig. 2. The camera image

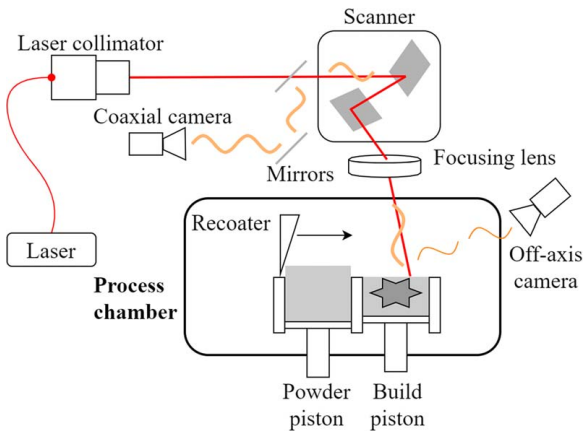

Fig. 1 Typical LPBF machine architecture

[1]Corresponding author.
[2]Also known as Selective Laser Melting (SLM) and Direct Metal Laser Melting (DMLM).

Manuscript received December 23, 2020; final manuscript received June 3, 2021; published online July 19, 2021. Assoc. Editor: Zhen Zhang.

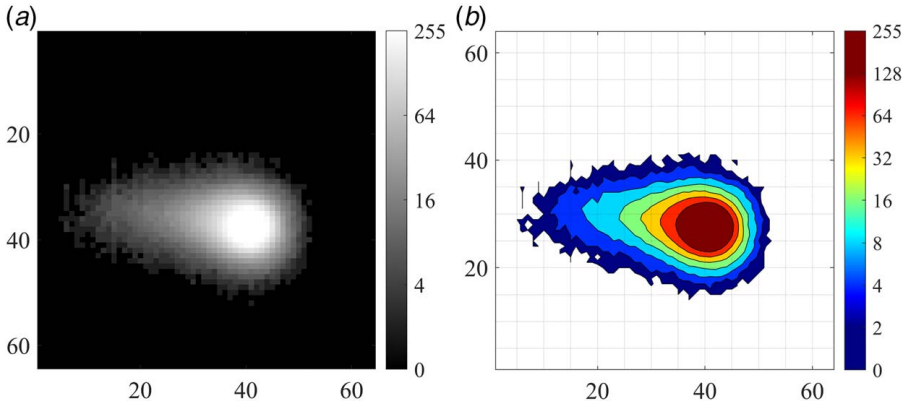

Fig. 2 An example of an acquired coaxial image. (*a*) Raw 8-bit gray scale image. Note the logarithmic intensity scale. (*b*) A contour plot of the same image. Different level sets are highlighted. Process parameters: laser power 250 W, scanning velocity 600 mm/s. Note that the NIR emission intensity is measured and not true temperature.

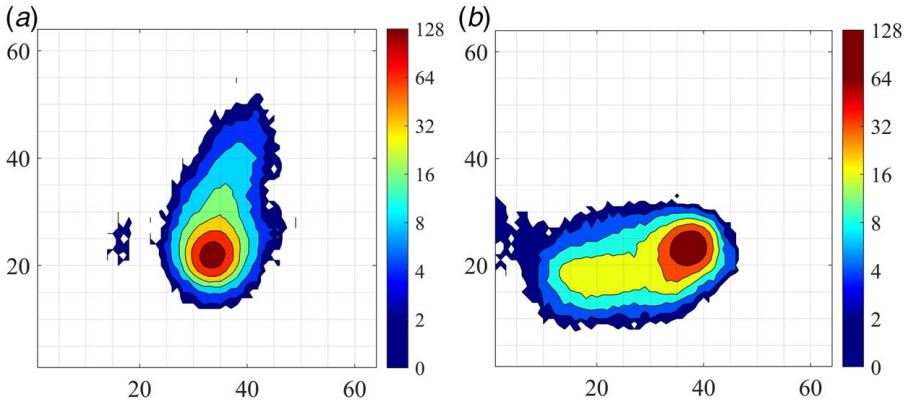

Fig. 3 Certain melt pool states are indistinguishable when a single-point measurement, e.g., a photodiode, is used. The total emission is 13,306 in (*a*) and 13,315 in (*b*) (the difference of 0.07%) while the melt pool condition is significantly different, e.g., "necking" of a level set 16.

acquisition is triggered by an external hardware signal that is synchronized with the laser operation.

While the sampling rate of the camera is lower than that of a photodiode (up to 100 kHz), NIR imaging can observe melt pool geometry which affects the part density and microstructure [15]. Meanwhile, a photodiode averages the thermal field it observes, and thus obscures the melt pool geometrical changes. Figure 3 shows two coaxial images acquired during a build. The images are noticeably different but the total emission in the field of view is the same for both images. A photodiode would not be able to distinguish these two melt pool states. In literature, Craeghs et al. followed up on their work [11] with a suggestion that, for control purposes, a camera-based control could be superior to a photodiode-based one, as the latter only provided "small improvement" [16]. Therefore, there is a need to study camera-based feedback.

The process monitoring and control logic is implemented via the in-house developed c++ code called from within America Makes software [17]. Unlike the commercial LPBF machines, the laser power on the testbed can be updated within individual scan lines. This is achieved by asynchronous calls to the scanner control library, overriding the power level determined from the build file. Laser power can be modified in both a feedback (based on images) and a feedforward (based on a pre-defined profile) manner. The control system presented in this letter uses melt pool image feedback to control the laser power, as shown in Fig. 4.

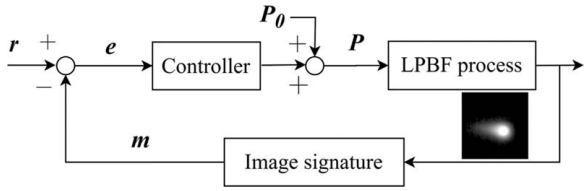

Fig. 4 Real-time melt pool control: $m(t)$ is the output signal extracted from the coaxial NIR image, $r(t)$ is the output reference to track, $e(t) = r(t) - m(t)$ is the output error, $P(t)$ is the commanded input laser power, and P_0 is the baseline laser power of 200 W

Figure 5 illustrates the synchronized interaction between the laser scanner control board, the melt pool camera, and the process control logic, implemented at the loop closure rate of 2 kHz. It takes less than 400 μs to retrieve the frame, process it, and issue the power update command.

3 Melt Pool Response Modeling

The output of the coaxial camera is inherently multidimensional (64×64 pixels). Naturally, different image signatures $m(\cdot)$ of

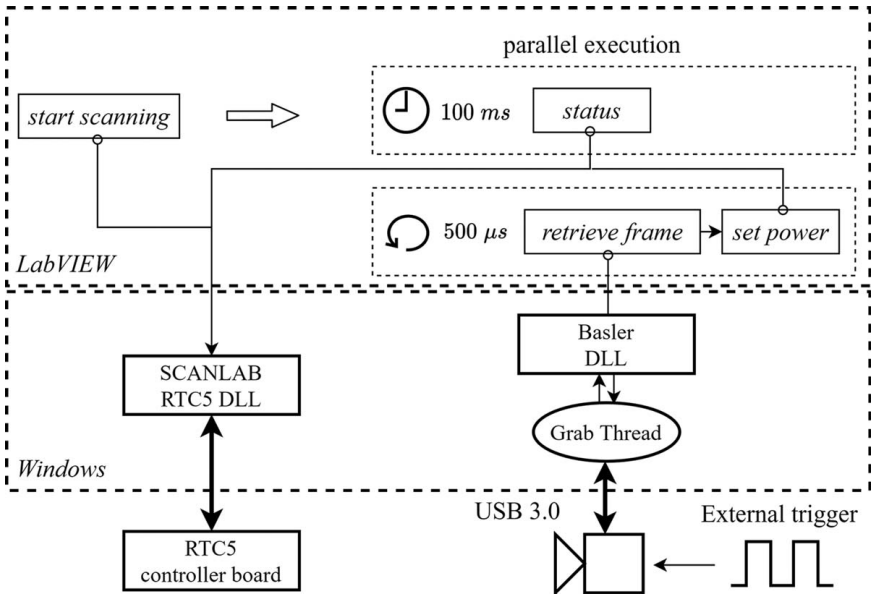

Fig. 5 LABVIEW, SCANLAB (scanner head), and Basler (coaxial NIR camera) hardware-software interfaces for real-time control

reduced dimensionality may be extracted from a coaxial image. Melt pool area, width, and length could be represented by a certain level set at a threshold α, as demonstrated by Fig. 2(*a*). Then, a transfer function (TF) from the input laser power to the selected signature can be systemically studied. A typical melt pool image can be described as a "droplet" with a bright center (Fig. 2). Consider an area encircled by the level set α:

$$C_\alpha = \sum_{r,c} 1[I(r, c) \geq \alpha] \tag{1}$$

where r and c are pixel coordinates, $I(r, c)$ is the intensity of the pixel at (r, c), α is a predefined threshold; $1[\cdots]$ stands for the indicator function, e.g., it is equal to 1 when its argument is true and is 0 otherwise. Then, the "droplet" can be represented by the area, in pixels, of a level set with a low threshold (e.g., C_{10}), while the "hot spot" in the image center can be linked to a larger threshold (e.g., C_{100}). In this work, only C_{100} will be considered.[3]

To the authors' best knowledge, this is the first report of an experimental image-based TF identification used for feedback control in LPBF. Based on the previous work by the authors [18], the dominant behavior of C_{100} can be described by a first-order model $P(s) = K/(\tau s + 1)$. A similar conclusion was made in Ref. [11]. Figure 6 shows the typical response of C_{100} signal to the changes in the input laser power and further supports the claim of the first-order behavior.

Previously, the authors have reported that the melt pool response varied with scanning speed and substrate [18]. It also evolved with layer number, settling after an initial transient of 10–20 layers. For this work, the authors identified TF for C_{100} at 800 mm/s scanning speed, as it is the speed setting used to produce the parts on the testbed. Two types of single scan line tests were performed to control for the layer transient:

(1) *Bare metal tracks*, where no powder is present and the laser scans a bare metal solid substrate.
(2) *Built-up part tracks*, where a layer of powder[4] is deposited on top of the LPBF-built substrate of sufficient (50 layers, e.g., 1.5 mm) thickness, so that the layer-related transient in TF parameters has converged.

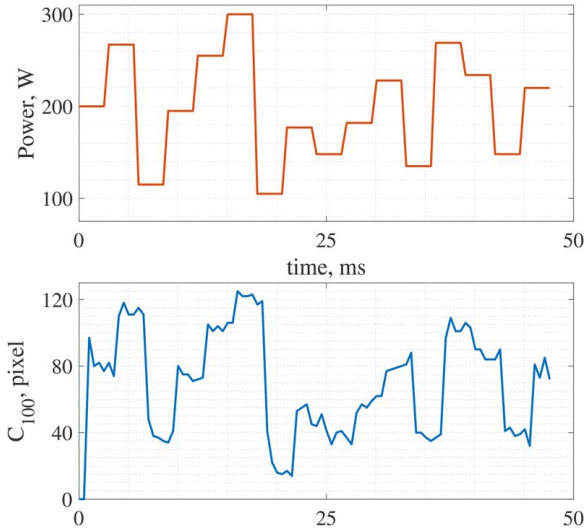

Fig. 6 The response of "hot spot" C_{100} to changes in laser power

The response of the "hot spot" C_{100} signature to the linearly ramping power is shown in Fig. 7. Signals from bare metal and built-up part tests differ in magnitude and slope. Moreover, the response to ramping power shows a concave shape, indicating non-linear plant behavior.

An effective feedback controller must address the variability of the plant with respect to scanning speed and substrate variation. In this work, such behavior is addressed via (1) a localized linear model around the nominal process parameters (on the testbed, 200 W for laser power and 800 mm/s for scanning speed are usually used) and (2) designing around the largest possible plant gain, i.e., worst-case gain margin. In future work, different process model structures can be investigated, e.g., a parameterized set of local models, or a fully non-linear input-output model, which is outside the scope of this letter.

[3]The selection of process signature here is not intended to be restrictive. A variety of signals were studied in this work and a representative signature was picked for clarity and brevity.
[4]CoCr powder is used throughout the work presented in this letter.

Figures 8(*a*) and 8(*b*) illustrate the models identified around the nominal process parameters. For the built-up part tracks, the gain was found to be around 0.47 pixel/W. Even though the built-up part test is more representative of the actual LPBF process, the model identified in bare metal tests was used for the control design because the plant gain was found to be larger.

The estimated parameters of C_{100} TF in bare metal tests were as follows: $K = 0.551 \pm 0.011$ pixel/W, $\tau = 447 \pm 15$ μs, with normalized root-mean-square error (NRMSE) of 0.43. The estimated time constant is in reasonable agreement with existing literature [4]. The estimate is based on the bare metal test with five lines scanned with different power profiles. The test was performed three times on separate bare metal plates, i.e., 15 lines total. Uncertainty is indicated by a standard deviation of the estimate.

4 Real-Time Melt Pool Feedback Control

In this work, the image-based feedback control of the melt pool is implemented, such that a desired melt pool reference is followed, as shown in Fig. 4. The remainder of the letter presents an experimental demonstration of a reference tracking on the single-track and then on the *multi-layer part* scale.

4.1 Controller Design. A time-varying reference tracking can be achieved with the proportional-integral controller, defined in serial form as $C(s) = K_p(1 + 1/sT_i)$, where $T_i = 0.0005$ in this work. Bare metal scans were used for the experimental controller verification. As illustrated in the previous section, scans on the bare metal result in the largest plant gain, while time constants in bare metal and built-up cases appear to be similar. Thus, a controller that has sufficient stability margins in the bare metal setting will have sufficient stability margins for the part-scale operation.

The closed-loop response is affected by delays (e.g., camera integration time, image transmission, actuation delay), which limit the achievable bandwidth. Conservatively, this delay T_d is assumed to be equal to one control-loop time-step, i.e., $T_d = 500$ μs, and the controller is designed to account for that.

The frequency response of the loop transfer function $L(s) = e^{-sT_d}P(s)C(s)$ can be evaluated analytically based on the nominal model from Sec. 3: the plant gain is 0.55 pixel/W, and the time constant is 447 μs. From Fig. 9, the gain margin for the controller with $K_p = 1.2$ W/pixel is at least 7 dB. However, oscillations at 400 Hz were observed in the output signal (Fig. 10(*a*)). Un-modeled dynamics or other effects could be responsible for this behavior and are currently being investigated. The oscillatory behavior is also evident in the track appearance, as illustrated by Fig. 11. The output of the closed-loop system with a tuned gain $K_p = 0.8$ W/pixel (gain margin of 11 dB, time delay margin of 1.4 ms at 145 Hz) is shown in Fig. 10(*b*). The output is free of oscillations, and the time-varying output reference is tracked well.

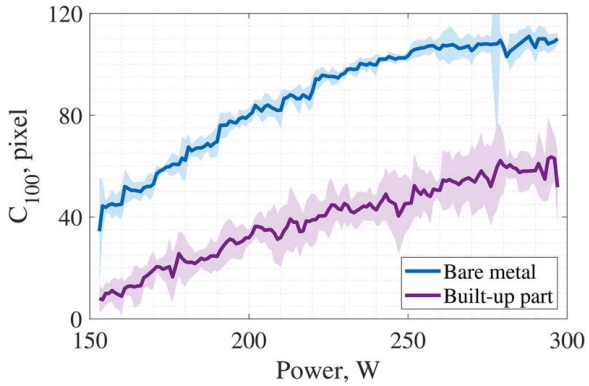

Fig. 7 The response of the C_{100} signature to the input power ramp. Each plot is a median of four ramp measurements. Shaded regions are constructed based on the interquartile ranges. Note the non-linearity in the observed trends.

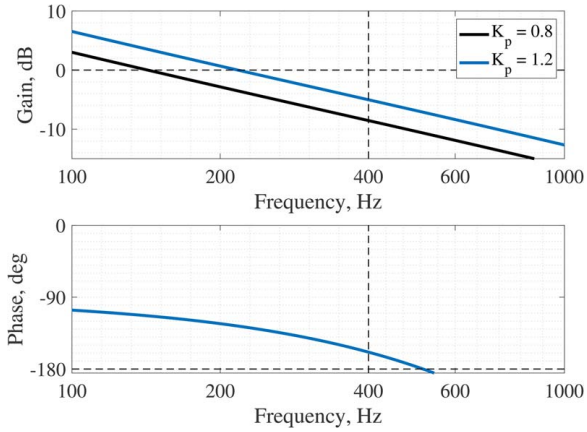

Fig. 9 The loop transfer function $L(s)$ from the laser power to C_{100}, on the bare metal at 800 mm/s. Note that the plot is zoomed on the crossover region. Top: nominally, the controller $K_p = 1.2$ has a positive gain margin. However, oscillations in the plant response are observed experimentally. Bottom: the phase response of the nominal $L(s)$, time delay $T_d = 500$ μs. The delay margin at 400 Hz is 140 μs.

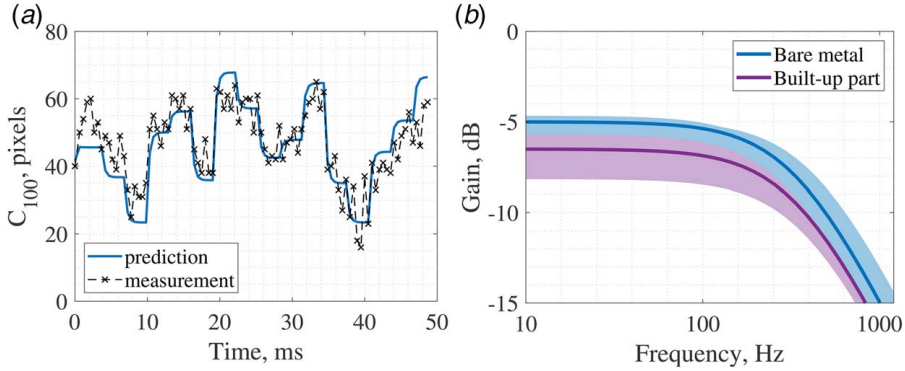

Fig. 8 The identified TFs, from the laser power to C_{100}, at 800 mm/s around 200 W. (*a*) The output of an identified first-order TF, compared against the validation data, in the built-up part test. (*b*) The magnitude response of the identified TFs for different underlying substrates. The gain is decreased in the built-up part case compared to the bare metal case.

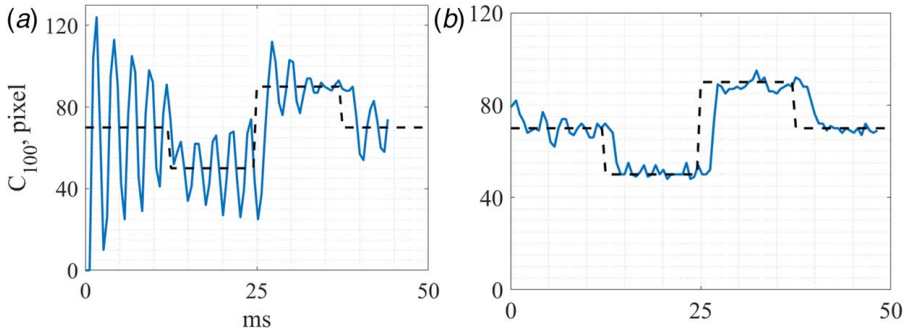

Fig. 10 The melt pool oscillation is observed experimentally when the controller gain K_p is sufficiently large. (*a*) With $K_p = 1.2$, an attempt at tracking of a time-varying C_{100} reference (black dashed line) leads to the output oscillation. (*b*) The controller with the reduced gain $K_p = 0.8$ successfully tracks the output reference.

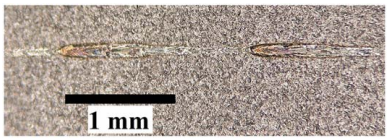

Fig. 11 Oscillation of the melt pool signature is observed experimentally when the controller gain K_p is too large. The observed oscillation (period of 2 mm at scanning speed of 800 mm/s) matches the observed frequency of the coaxial signal oscillation (400 Hz). Only two periods of oscillation are shown to highlight the effect, as the width oscillation is not evident at larger magnifications able to capture all 40 mm of the track.

4.2 Part-Scale Melt Pool Regulation. The feedback controller designed in Sec. 4.1 was then applied to the LPBF process on a part-level scale. To ensure no transient layer-to-layer behavior, 50 layers of substrate were built first. Then, four identical square geometries of 15 × 15 mm cross-section were built in parallel: two with a constant laser power (open-loop), and another two under the feedback control. The nominal scanning parameters were as follows: laser power 200 W, scanning speed 800 mm/s, hatch spacing 90 μm. The layers were hatched at 0 deg, 45 deg, and 90 deg. Layers 1, 4, 7 $\cdots$ were scanned vertically, layers 2, 5, 8 $\cdots$ were scanned diagonally, and layers 3, 6, 9 $\cdots$ were scanned horizontally. A total of 10 layers were built, and more than 240,000 unique coaxial images were acquired as the result.

Compared to the data presented in the previous sub-section, an introduction of powder increases the variability in the output signal. To combat the high-frequency powder-related effects, a low pass filter with a cut-off frequency of 200 Hz was used to filter the C_{100} signature. The filter was implemented digitally as an infinite impulse response filter of the form

$$C_f(k) = 0.4665 C_{100}(k) + 0.5335 C_f(k-1) \tag{2}$$

where C_f is the filtered output signal. Thus, the output error was $e_f(k) = r - C_f(k)$. The output reference was set to $r = 35$. In the future, the signature and the reference value should be selected according to the desired melt pool size, shape, or other metrics.

A detailed analysis of this data is not the subject of this letter. However, a brief discussion is presented below.

Figure 12 shows the filtered output signature C_f as a function of the spatial coordinates x, y on the build plate. Four squares from a single layer are shown. The bottom row squares were built with the feedback controller regulating the output, while the top row squares were built in the open-loop mode. The output time series for the OL1 and FB1 squares are shown in Fig. 13, while Fig. 14(*a*) shows the feedback input signal corresponding to Fig. 13(*b*). From Fig. 13(*b*), it is clear that the feedback control

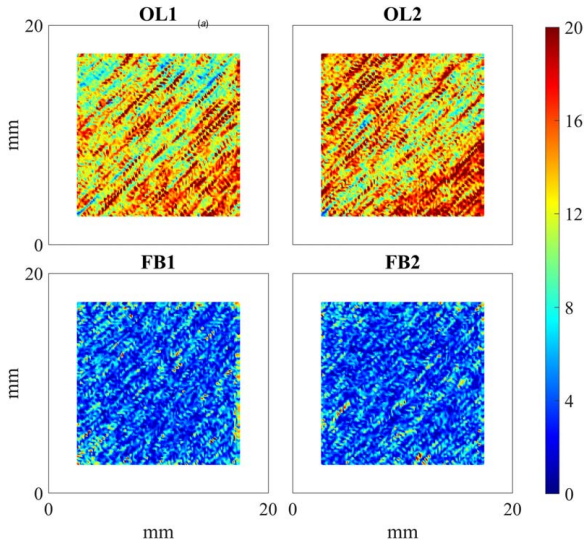

Fig. 12 Error $e_f(x, y) = |r - C_f(x, y)|$ in the image signature C_{100}, plotted for layer 8, for two controlled (FB) and two open-loop (OL) squares

successfully regulated the plant's output, while the open-loop output signal deviated from a constant level.

In addition, signals acquired from the two open-loop squares clearly differ even within the same layer. For example, the OL2 square has more locations with higher values of C_f than the OL1 square. A plethora of reasons could cause such differences in open-loop parts, e.g., variations in the powder re-coating quality, spatter from the parts landing on the build surface, or thermal interactions between the parts. Meanwhile, the feedback-controlled signals appear to match more closely. The feedback control significantly reduced the error norm for all 10 layers, as shown in Fig. 14(*b*). Based on these findings, real-time feedback control could result in better part-to-part consistency.

For the OL squares, an increase of the coaxial signature is observable in proximity to the corners. This effect is possibly caused by the diagonal scanning pattern at 45 deg hatch angle, where the melt pool returns to the previously heated area at an ever-increasing rate. Again, no signature increase of such kind is observable in the feedback-controlled parts.

A detailed analysis of the data from the feedback-controlled builds, as well as an investigation of the influence of the feedback control on part quality metrics, is necessary as follow-up work. In the context of this letter, the applicability of the designed system for the real-time image-based control in LPBF was successfully demonstrated.

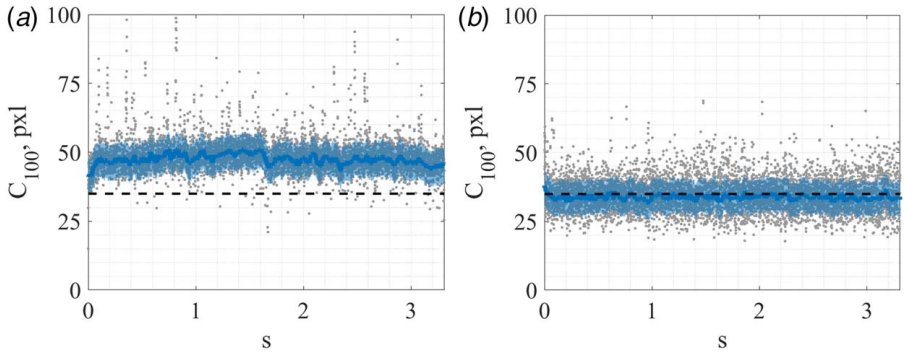

Fig. 13 Filtered signature C_f as measured during the scanning of (*a*) OL1 and (*b*) FB1 squares from Fig. 12. Frames acquired during the laser re-positioning ("jumps") are omitted. A filtered trend (median, window size 100) is shown with the solid line, with the C_f data in the background. The shaded band indicates the ±1 standard deviation of C_f.

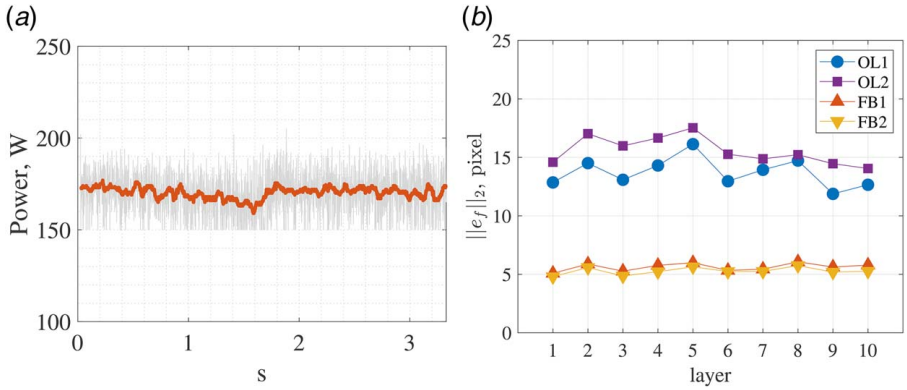

Fig. 14 (*a*) The input laser power corresponding to Fig. 13(*b*). Filtered trend (same filter as in Fig. 13(*b*) is shown with the solid line. (*b*) The evolution of the 2-norm of the error e_f with layer number. Both feedback-controlled squares exhibit reduced error for all layers.

5 Conclusion

The real-time LPBF control system presented in this letter enables easy control algorithm development and implementation, e.g., image-based process monitoring and feedback control of the melt pool signature. The system allows for real-time laser power modulation in both a feedforward and a feedback manner.

The system's capabilities for empirical modeling were experimentally demonstrated. Prescribed input signals were used to identify empirical models for different reductions of the multidimensional image data. Models' dependencies on process parameters and other variables, e.g., substrate material, were stated. At 2 kHz sampling, the system enables real-time implementation of feedback control schemes. A time-varying reference tracking was successfully experimentally demonstrated on a single-track scale. Furthermore, the melt pool image signature was experimentally regulated to the desired level on a *part* scale, in real-time, using feedback control.

Potential directions for future work include process control for the LPBF builds with complicated geometries, targeting improved process outcomes and better part quality. Process disturbances, e.g., heat buildup or scanning-induced thermal disturbances on a part scale, are also being investigated.

Acknowledgment

This work is supported by NSF Data-Driven Cyberphysical Systems Award #1645648 and by the State of New York ESD/NYSTAR program.

Conflict of Interest

There are no conflicts of interest.

References

[1] Grasso, M., and Colosimo, B. M., 2017, "Process Defects and *In Situ* Monitoring Methods in Metal Powder Bed Fusion: A Review," Meas. Sci. Technol., **28**(4), pp. 1–25.

[2] Tapia, G., and Elwany, A., 2014, "A Review on Process Monitoring and Control in Metal-Based Additive Manufacturing," ASME J. Manuf. Sci. Eng., **136**(6), pp. 1–10.

[3] Everton, S. K., Hirsch, M., Stavroulakis, P. I., Leach, R. K., and Clare, A. T., 2016, "Review of In-Situ Process Monitoring and In-Situ Metrology for Metal Additive Manufacturing," Mater. Des., **95**, pp. 431–445.

[4] Mazzoleni, L., Demir, A. G., Caprio, L., Pacher, M., and Previtali, B., 2020, "Real-Time Observation of Melt Pool in Selective Laser Melting: Spatial, Temporal and Wavelength Resolution Criteria," IEEE Trans. Instrum. Meas., **69**(4), pp. 1179–1190.

[5] Yeung, H., Lane, B., and Fox, J., 2019, "Part Geometry and Conduction-Based Laser Power Control for Powder Bed Fusion Additive Manufacturing," Addit. Manuf., **30**, pp. 1–13.

[6] Yeung, H., Yang, Z., and Yan, L., 2020, "A Meltpool Prediction Based Scan Strategy for Powder Bed Fusion Additive Manufacturing," Addit. Manuf., **35**, pp. 1–8.

[7] Wang, Q., Michaleris, P. P., Nassar, A. R., Irwin, J. E., Ren, Y., and Stutzman, C. B., 2020, "Model-based Feedforward Control of Laser Powder Bed Fusion Additive Manufacturing," Addit. Manuf., **31**, pp. 1–14.

[8] Vasileska, E., Demir, A. G., Colosimo, B. M., and Previtali, B., 2020, "Layer-Wise Control of Selective Laser Melting by Means of Inline Melt Pool Area Measurements," J. Laser. Appl., **32**(2), pp. 1–10.

[9] Shkoruta, A., Caynoski, W., Mishra, S., and Rock, S., 2019, "Iterative Learning Control for Power Profile Shaping in Selective Laser Melting," IEEE International Conference on Automation Science and Engineering (CASE), Vancouver, BC, Canada, Aug. 22–26, pp. 655–660.

[10] Kruth, J.-P., Mercelis, P., Vaerenbergh, J. V., and Craeghs, T., 2007, "Feedback Control of Selective Laser Melting," Proceedings of the 3rd International Conference on Advanced Research in Virtual and Rapid Prototyping, Leiria, Portugal, Sept. 24–29, pp. 1–7.
[11] Craeghs, T., Bechmann, F., Berumen, S., and Kruth, J.-P., 2010, "Feedback Control of Layerwise Laser Melting Using Optical Sensors," Phys. Procedia., **5**(2), pp. 505–514.
[12] Renken, V., Freyberg, A. V., Schünemann, K., Pastors, F., and Fischer, A., 2019, "In-Process Closed-Loop Control for Stabilising the Melt Pool Temperature in Selective Laser Melting," Prog. Addit. Manuf., **4**, pp. 411–421.
[13] Shkoruta, A., Mishra, S., and Rock, S., 2019, "Coaxial Near-Infrared Camera Measurements for Process Control in Selective Laser Melting," Proceedings of the 34th ASPE Annual Meeting, Pittsburgh, PA, Oct. 28–Nov. 1, pp. 54–59.
[14] Doubenskaia, M., Grigoriev, S., Zhirnov, I., and Smurov, I., 2016, "Parametric Analysis of SLM Using Comprehensive Optical Monitoring," Rapid. Prototyp. J., **22**(1), pp. 40–50.
[15] King, W. E., Anderson, A. T., Ferencz, R. M., Hodge, N. E., Kamath, C., Khairallah, S. A., and Rubenchik, A. M., 2015, "Laser Powder Bed Fusion Additive Manufacturing of Metals: Physics, Computational, and Materials Challenges," Appl. Phys. Rev., **2**(4), pp. 1–53.
[16] Craeghs, T., Clijsters, S., Yasa, E., Bechmann, F., Berumen, S., and Kruth, J.-P., 2011, "Determination of Geometrical Factors in Layerwise Laser Melting Using Optical Process Monitoring," Optics Lasers Eng., **49**(12), pp. 1440–1446.
[17] America Makes. 4039 Development & demonstration of open-source protocols for powder bed fusion AM, https://www.americamakes.us/portfolio/4039-development-demonstration-open-source-protocols-powder-bed-fusion-additive-manufacturing-pbfam Accessed June 2, 2020.
[18] Shkoruta, A., Mishra, S., and Rock, S., 2020, "An Experimental Study on Process Modeling for Selective Laser Melting*," 2020 American Control Conference (ACC), Denver, CO, July 1–3, pp. 467–473.